

RORem: Training a Robust Object Remover with Human-in-the-Loop

Ruixin Li^{1,2}, Tao Yang³, Song Guo⁴, Lei Zhang^{1,2*}

¹The Hong Kong Polytechnic University, ²OPPO Research Institute, ³ByteDance

⁴The Hong Kong University of Science and Technology

Abstract

Despite the significant advancements, existing object removal methods struggle with incomplete removal, incorrect content synthesis and blurry synthesized regions, resulting in low success rates. Such issues are mainly caused by the lack of high-quality paired training data, as well as the self-supervised training paradigm adopted in these methods, which forces the model to in-paint the masked regions, leading to ambiguity between synthesizing the masked objects and restoring the background. To address these issues, we propose a semi-supervised learning strategy with human-in-the-loop to create high-quality paired training data, aiming to train a Robust Object Remover (RORem). We first collect 60K training pairs from open-source datasets to train an initial object removal model for generating removal samples, and then utilize human feedback to select a set of high-quality object removal pairs, with which we train a discriminator to automate the following training data generation process. By iterating this process for several rounds, we finally obtain a substantial object removal dataset with over 200K pairs. Fine-tuning the pre-trained stable diffusion model with this dataset, we obtain our RORem, which demonstrates state-of-the-art object removal performance in terms of both reliability and image quality. Particularly, RORem improves the object removal success rate over previous methods by more than 18%. The dataset, source code and trained model are available at <https://github.com/leeruixin/RORem>.

1. Introduction

Object removal aims to inpaint user-specified masked objects with realistic background, which is an important task in the fields of photography, advertising and film industry [6, 43, 68]. Various CNN-based [31, 37, 41, 54] and transformer-based [7, 19, 26, 50] networks have been developed, aiming to understand the image global content and thereby enhance the coherence of the inpainting process.

*Corresponding author. This work is supported by the PolyU-OPPO Joint Innovative Research Centre.

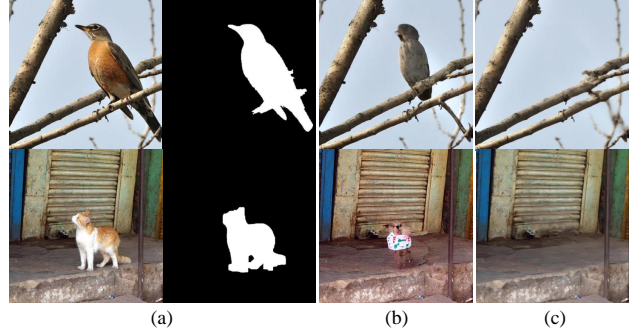


Figure 1. Given an input image and a mask (see (a)), existing object removal methods such as PowerPaint [72] may inpaint the masked regions with other objects (see (b)), while our method can successfully remove the masked objects (see (c)).

GAN-based approaches [21, 32, 41, 57] have demonstrated their efficacy in object removal by employing adversarial loss in the training process. Recent advancements have further leveraged the generative priors from large-scale pre-trained diffusion models [12, 22, 24, 35, 48, 59, 60, 64] to facilitate the inpainting of masked regions.

Despite the commendable results, previous methods frequently encounter challenges such as incomplete removal, erroneous content synthesis and blurry synthesized regions, culminating in a low success rate. The primary reason for these shortcomings lies in the prevalent reliance on a self-supervised training paradigm using random masks [42, 54, 59], which compels the model to inpaint the masked regions using the original content, thereby inducing ambiguities during testing. As shown in Fig. 1(b), for example, when the bird or cat is masked, the training paradigm obliges the model to reconstruct the bird/cat based on the unmasked contents, whereas our objective is to remove the object and restore the background. To mitigate this ambiguity, high-quality paired training data containing images before and after the object’s presence are essential. Recent efforts have sought to construct such paired datasets, either by capturing images [47, 59] in real-world scenarios or by synthesizing realistic data [56, 64]. Nonetheless, the size, diversity and quality of these datasets remain constrained, limiting the object removal performance.

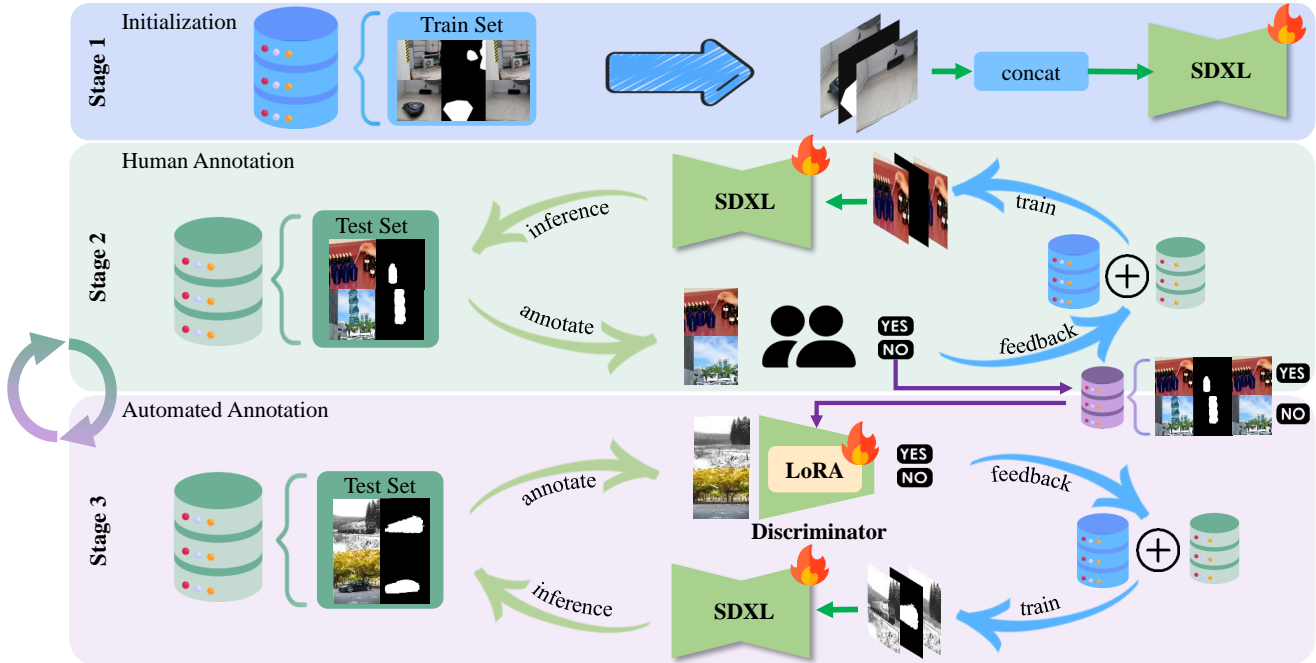


Figure 2. Overview of our training data generation and model training process. In stage 1, we gather 60K training triplets from open-source datasets to train an initial removal model. In stage 2, we apply the trained model to a test set and engage human annotators to select high-quality samples to augment the training set. In stage 3, we train a discriminator using the human feedback data, and employ it to automatically annotate high quality training samples. We iterate stages 2&3 for several rounds, ultimately obtaining over 200K object removal training triplets as well as the trained model.

To address these challenges, we propose a semi-supervised learning scheme that leverages human feedback to generate high-quality paired training data, as illustrated in Fig. 2. We initially collect 60K training triplets from two open-source datasets: a real video removal dataset RORD [47] captured by photographers, and a synthesized dataset MULAN [56] based on COCO [28] and LAION aesthetics [49]. Each triplet consists of the original image, the edited image with certain items removed, and the corresponding mask. With this dataset, we train a Stable Diffusion XL (SDXL) [42] based inpainting model. This initial model can only achieve a success rate less than 50% due to the limited data size and category diversity. Consequently, we introduce a human-in-the-loop approach to augment the training data. We randomly select the images and masks from the OpenImages dataset [20], and use the initially trained model to generate the object removed samples. Then, human annotators are invited to select high-quality object removal pairs, which are then added to the training dataset. Meanwhile, we use the human feedback data to train a discriminator that is aligned with human preference in judging high-quality object removal pairs. This discriminator enables us to automate the subsequent training data generation process. By iterating the human- and automated-annotation stages for several rounds, we obtain an object removal dataset comprising over 200K pairs across diverse categories. In ad-

dition, we compile a small high-resolution dataset for final fine-tuning to enhance the output image quality.

With our collected dataset, we fine-tune the SDXL inpainting model to obtain a **Robust Object Remover**, referred to as **RORem**. As shown in Fig. 1(c), RORem can completely remove the targeted objects and reproduce clear background. Considering that the inference efficiency is crucial for practical usage (note that some approaches cost over 20 seconds to edit a single image), we introduce trainable LoRA layers into RORem and leverage distillation technologies [36] to improve editing efficiency. As a result, our RORem can complete the removal process in four diffusion steps (less than 1 second). Extensive experiments demonstrate that RORem outperforms previous methods in terms of both objective metrics and subjective evaluations. Notably, for metrics such as the success rate evaluated by human subjects, RORem surpasses the second-best methods by 18% with faster inference speed.

2. Related Work

Image Inpainting. Early image inpainting methods predominantly synthesize the training data by randomly masking regions from images. Taking the masked image as inputs, the model learns to reproduce the original masked content. Under this paradigm, early endeavors often utilize the

encoder-decoder framework to accomplish the inpainting task [37, 41, 54], and U-Net [46] is widely used as the backbone [29, 31, 61, 67]. In recent years, transformer-based networks have garnered increasing attention in inpainting for their intrinsic capability to complete masked patches [5, 7, 19, 26, 50, 66, 71]. In addition, researchers have also investigated the impact of losses on inpainting performance. Beyond the conventional L_1 and L_2 losses, perceptual loss has been employed to extract high-level semantic features [23, 29, 53, 62]. The GAN [11] network has also been adopted for inpainting by integrating adversarial loss and trainable discriminators [30, 41, 63, 65].

Recently, diffusion models have revolutionized the field of image generation [3, 9, 15, 42, 45, 52]. Leveraging the powerful generative priors, recent works have adapted the pre-trained text-to-image (T2I) models for inpainting by employing the self-supervised training paradigm [35, 42, 48, 58]. While exhibiting their efficacy across various inpainting tasks (e.g., image completion, object removal, content replacement), these methods lack reliability in large-scale tests. This limitation primarily stems from the self-supervised training paradigm, which compels the model to inpaint the masked regions utilizing the original content, which induces ambiguity during the testing phase.

Object Removal. Object removal can be viewed as a sub-task of image inpainting, aiming at erasing the selected objects from the given image. Therefore, many inpainting models can be directly employed for object removal tasks [19, 37, 50, 54, 71]. Among them, those stable diffusion (SD) [51, 59, 64, 72] based methods are predominantly utilized, which can be categorized into two categories. 1) *Inversion-based methods* [13, 14, 17, 25, 39], which first convert the input image into a latent noise code based on inversion techniques [25, 39, 52], and then modify certain intermediate features (e.g., dropping the attention feature of specific words) to yield the edited output. However, the quality of removal outputs cannot be assured in many instances, and the model efficiency is compromised due to inversion process. 2) *Training-based methods*, which typically fine-tune pretrained SD models. They may utilize learnable embeddings or text prompts as auxiliary information to facilitate the object removal process [4, 10, 51, 70, 72]. Some recent studies have transitioned the self-supervised training paradigm to a supervised training approach by generating removal data pairs [47, 51, 59, 64]. However, neither the datasets and models are available to the public [51, 59, 70], nor the data quality and quantity are sufficient to train a reliable removal model [38, 56, 64].

3. Proposed Method

Given a source image \mathbf{x}_s and a mask \mathbf{m} , we aim to train a generative model G_θ to produce an edited image \mathbf{x}_e so that the unmasked region of \mathbf{x}_e , represented as \mathbf{x}_e^t

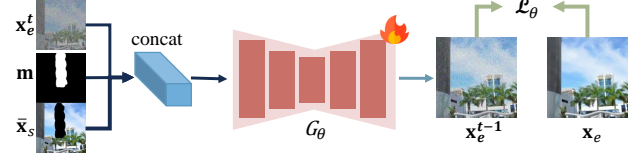


Figure 3. We finetune the pre-trained SDXL-inpainting model with the standard diffusion training loss. We concatenate triplets data together as the model inputs. The same training paradigm is employed across all the three stages.

($1 - \mathbf{m}$), remains the same as \mathbf{x}_s , while the masked region, denoted as $\mathbf{x}_e \cdot \mathbf{m}$, is filled with background. G_θ is conventionally trained in a self-supervised manner, relying solely on training pairs of $(\mathbf{x}_s, \mathbf{m})$. However, the trained model tends to reconstruct \mathbf{x}_s from the masked image $\mathbf{x}_s \cdot (1 - \mathbf{m})$, resulting in ambiguity between synthesizing masked objects and restoring background. High-quality training triplets $(\mathbf{x}_s, \mathbf{m}, \mathbf{x}_e)$ can be employed to significantly enhance the removal performance since the true removal result \mathbf{x}_e can circumvent the dilemma associated with the self-supervised training paradigm. Acknowledging the scarcity of high-quality triplet data, we propose a human-in-the-loop paradigm to facilitate the data generation while concurrently training the model. As illustrated in Fig. 2, our proposed framework is composed of an initialization stage, and human annotation stage and an automated annotation stage. The details of each stage are described in the following subsections.

3.1. Model Initialization

In contrast to prior works that utilize $(\mathbf{x}_s, \mathbf{m})$ as training pairs, our approach necessitates high-quality triplet data $(\mathbf{x}_s, \mathbf{m}, \mathbf{x}_e)$ for effective model training. However, such triplet data are scarce to obtain. The recent work Object-Drop [59] provides 2K triplets by employing photographers to capture images before and after the object is removed; however, the limited quantity poses challenges on model training, and neither the dataset nor the trained model is publicly available. Upon thorough evaluation of the existing datasets, we ultimately select two open-source datasets, RORD [47] and Mulan [56], to initialize our model training.

The RORD dataset comprises about 3K short video clips captured with a fixed camera. Each video features a foreground object that moves throughout the video, with corresponding masks provided. Subsequently, a static background image of the same scene, devoid of moving objects, is captured. We extract 5 frames from each video and utilize the static image as the object removal result, yielding a total of 15K high-quality removal triplets. While the quality of this dataset is commendable, over 2.5K videos pertain to human removal cases, restricting the model's capacity to other scenes. Therefore, we incorporate a synthetic dataset, Mulan, whose images are from COCO2017 [28] and Laion-

Aesthetics V6.5 [49]. Originally designed for layered image generation, Mulan contains extracted foreground objects and inpainted background. Compared to RORD, the Mulan dataset exhibits greater diversity in categories, but its removal quality is lower.

Our training paradigm adheres to the diffusion model training pipeline, as illustrated in Fig. 3. In specific, we inject noise to the removal result \mathbf{x}_e as $\mathbf{x}_e^t = \alpha_t \cdot \mathbf{x}_e + \sigma_t \cdot \epsilon$, where $t \sim [0, T]$ is the diffusion timestep, $\epsilon \sim \mathcal{N}$ is the Gaussian noise, α_t, σ_t are two constants depending only on the noise scheduler and timestep t . A denoising network G_θ , initialized by a pre-trained SDXL inpainting model [42], is fine-tuned to learn the denoising process. To provide additional context regarding the background and the removal region, we concatenate the unmasked region of the source image, defined as $\bar{\mathbf{x}}_s = \mathbf{x}_s \cdot (1 - \mathbf{m})$, along with the mask \mathbf{m} to the noisy input \mathbf{x}_e^t . While ObjectDrop [59] suggests that satisfactory results can be achieved by concatenating the complete source image \mathbf{x}_s and the mask \mathbf{m} , it may result in transparent object residuals in the removal output. In contrast, we find that masking the removal region prior to concatenation can significantly enhance the robustness of object removal model. Our final loss function is defined as follows:

$$\mathcal{L}_\theta = \mathbb{E}_{t \sim [0, T], \epsilon \sim \mathcal{N}} \left[\|\epsilon - G_\theta(\mathbf{x}_e^t, \bar{\mathbf{x}}_s, \mathbf{m}, t)\|_2^2 \right]. \quad (1)$$

3.2. Human Annotation

While finetuning the SDXL-inpainting model with the initial dataset can improve the removal robustness, the success rate is hard to exceed 50% due to the limited number and quality of training samples. We implement a human-in-the-loop process to further enhance the training dataset and our model. Specifically, we randomly select images from the OpenImages dataset [20] to construct a test set, which contains 10K pairs. Each pair consists of a source image, denoted by \mathbf{x}_s^i , and a mask, denoted by \mathbf{m}^i . During the selection process, we exclude certain terms (*e.g.*, clothes, body) to prevent from acquiring erroneous knowledge. Additionally, if the number of instances for a particular class exceeds 500, we will stop the sampling of this class. By applying the initial removal model to this test set, we obtain 10K removal results, denoted by \mathbf{x}_e^i , which encompass both high-quality and low-quality removal cases.

To filter out low-quality removal cases, we engage 10 human annotators to evaluate the removal images. For each case, the annotators are provided with the source image, the mask image, and the edited image, and they are asked to assign the removal result by a label y^i , whose value is either “yes” (*i.e.*, high quality) or “no” (*i.e.*, low quality). This process enables us to compile a quadruple set $(\mathbf{x}_e^i, \mathbf{x}_s^i, \mathbf{m}^i, y^i)$. During the annotation process, those cases with incomplete removals, blurry removal regions, and in-

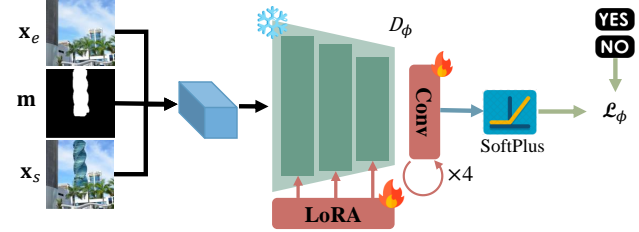


Figure 4. Training of the discriminator for automated data annotation. We use the down and middle blocks of SDXL-inpainting model as the base model, introduce trainable LoRA layers into it, and add several convolutional layers after them. Human feedback data are utilized to train the LoRA and convolutional layers.

correct inpainting contents are all classified as failure cases. With human feedback, we can expand the training dataset with high-quality removal samples and retrain our model G_θ . Specifically, we collect 4182, 7008 and 6133 valid removal samples, respectively, in three rounds of human annotations, as shown in Tab. 1.

3.3. Automated Annotation

While human annotation can output high-quality removal samples, it is very costly and time-consuming. To collect data more cost-effectively, we propose to use the quadruple set $(\mathbf{x}_e^i, \mathbf{x}_s^i, \mathbf{m}^i, y^i)$ collected in the human annotation process to train a discriminator, denoted by D_ϕ , and use it to perform automated annotation. The architecture and training framework of discriminator D_ϕ are depicted in Fig. 4. We leverage the down and middle blocks of pre-trained SDXL-inpainting model [42] as the backbone, and introduce trainable LoRA [16] layers (with rank 4) to fine-tune it. Additionally, we introduce several convolutional layers to transform the middle block output into a confidence score ranging from 0 to 1. The training loss of D_ϕ is:

$$\mathcal{L}_\phi = \frac{1}{N} \sum_{i=1}^N \|D_\phi(\mathbf{x}_e^i, \mathbf{x}_s^i, \mathbf{m}^i) - y^i\|_2^2. \quad (2)$$

The discriminator takes the object removed image \mathbf{x}_e , the source image \mathbf{x}_s and the mask image \mathbf{m} as input, and uses the human annotated label as the supervision output. More details on the training of D_ϕ can be found in Sec. 4.3.

Once D_ϕ is trained, we employ the same sampling principle as in human annotation to collect another test set from the Openimage dataset, and apply the removal model G_θ retrained in the human annotation stage to this test set. The discriminator D_ϕ is used to label the removal results. To ensure the quality of automatic labeling, only those removal samples whose confidence scores are higher than 0.9 are selected as the successful cases and added to the training set.

We iterate the human and automated annotation stages for 3 rounds to increase the size and diversity of our training

Round	Datasets	No. of Test Images	No. of Selected Pairs	Total Train Size	Success Rate	PSNR
Base Model	—	—	—	—	7.6	25.72
Initialization	RORD&Mulan	61,565	61,565	61,565	38.6	28.41
Human (Round 1)	OpenImage	10,000	4,182	65,747	47.8	28.63
Automation (Round 1)	OpenImage	30,000	20,634	86,381	55.6	28.60
Human (Round 2)	OpenImage	10,000	7,008	93,389	61.4	28.70
Automation (Round 2)	OpenImage	80,000	51,099	144,488	67.2	28.75
Human (Round 3)	OpenImage	10,000	6,133	150,621	71.8	28.77
Automation (Round 3)	OpenImage	95,204	49,313	199,934	75.4	28.78
Final Stage	DIV2K&Flicker2K	—	1,200	201,134	76.2	31.10

Table 1. The details of our constructed dataset throughout the several rounds of annotations. We employ SDXL-inpainting as the initial object removal model and fine-tune it during our dataset construction process.

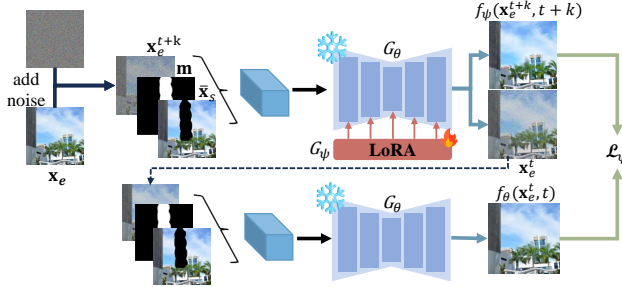


Figure 5. Efficient model distillation. We integrate trainable LoRA layers into the trained RORRem model, and fine-tune it by adapting the pipeline of latent-consistency-model (LCM) under the guidance of original RORRem. The distilled model can perform high-quality object removal in four diffusion steps.

set. The numbers of test images and selected pairs in each round are shown in Tab. 1. After each round of human annotation, we fine-tune the discriminator to improve its discrimination performance. After the final stage of automated annotation and re-training, we compile a small dataset of 1200 high-quality removal pairs. The images of this dataset are selected from the DIV2K [2] and Flicker2K [55] datasets, which have 2K resolution. SAM [18] is used to generate the masks. We utilize this dataset to conduct the final 20K fine-tuning steps, aiming at enhancing the overall image quality of removal results. As shown in Tab. 1, while further improving a little the removal success rate, the fidelity metric PSNR is significantly improved.

3.4. Model Distillation

While our RORRem can produce promising removal outcomes, it takes tens of diffusion steps to complete the removal process, which incurs a running time of over 4 seconds per image on an A100 GPU (50 steps). To improve time efficiency, we propose to introduce trainable LoRA layers with a rank of 64 into RORRem, and adopt distillation

techniques [36] to distill a four-step RORRem. The distillation process is illustrated in Fig. 5.

For the convenience of expression, we denote by $G_\theta(\mathbf{x}_e^t, t)$ the predicted noise $G_\theta(\mathbf{x}_e^t, \bar{\mathbf{x}}_s, \mathbf{m}, t)$. To perform distillation, we first define a function $f(\mathbf{x}_e^t, t)$, which aims to estimate the clear image from $G_\theta(\mathbf{x}_e^t, t)$. The function $f(\mathbf{x}_e^t, t)$ is defined as follows:

$$f_\theta(\mathbf{x}_e^t, t) = c_{skip}(t)\mathbf{x}_e^t + c_{out}(t)\frac{\mathbf{x}_e^t - \sigma_t G_\theta(\mathbf{x}_e^t, t)}{\alpha_t}, \quad (3)$$

where scalars $c_{skip}(t)$ and $c_{out}(t)$ depend solely on the noise scheduler and the timestep t [15, 52]. As illustrated in Fig. 5, we denote by f_θ and f_ψ the above functions associated with the original RORRem G_θ and the fine-tuned RORRem with LoRA layers G_ψ , respectively. We expect that the output image of f_ψ should be as close to that of f_θ as possible, which can be achieved by employing the following distillation loss function:

$$\mathcal{L}_\psi = \mathbb{E}_{t \sim [0, T]} \|f_\theta(\mathbf{x}_e^{t+k}, t+k) - f_\psi(\hat{\mathbf{x}}_e^t, t)\|_2^2, \quad (4)$$

where $\hat{\mathbf{x}}_e^t$ is estimated by denoising \mathbf{x}_e^{t+k} for k steps based on DDIM sampling [52], represented as $\hat{\mathbf{x}}_e^t = DDIM_\theta(\mathbf{x}_e^{t+k}, \bar{\mathbf{x}}_s, \mathbf{m}, t+k)$. In our experiments, we set $k = 20$, which is consistent with LCM [36]. All parameters θ in our RORRem are fixed throughout the distillation process. Unlike the original LCM, we set the text condition as null \emptyset and the classifier-free guidance scale to 1, as text condition input is unnecessary in the our task of object removal process. This modification not only reduces memory requirements but also enhances the efficiency during both training and inference. We fine-tune the LoRA parameters ψ for 30,000 steps utilizing our constructed removal dataset, enabling us to complete the removal process in four steps with an average runtime of 0.50 second on an A100 GPU.

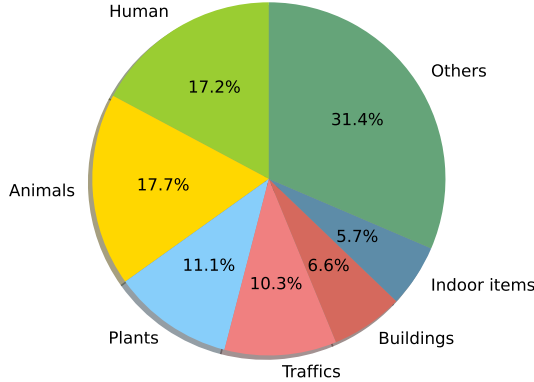


Figure 6. The category distribution of our constructed dataset.

4. Experiment

4.1. Experiment Setting

Training and Testing Datasets. As described in Sec. 3, we utilize RORD [47] and Mulan [56] as our initial training datasets. Consequently, we sample images from the OpenImage dataset [20], filtering out images by specific keywords (*e.g.*, clothes, human body) to mitigate unreasonable removal cases and excluding instances with excessively small ($< 3\%$) or large ($> 70\%$) mask regions. For each sampled image from the OpenImage dataset, we resize its shortest side to 512 pixels and center-crop the image to a resolution of 512×512 for training. We employ both human and automatic annotations to augment our training dataset, ultimately yielding a total of 201,134 removal pairs, as summarized in Tab. 1. The category distribution of our final training dataset is illustrated in Fig. 6.

We evaluate RORem alongside other competing methods using two test sets, which have the same image scenes but under two resolutions: 512×512 and 1024×1024 . Both test sets have 500 pairs of original images and their corresponding masks. The test images are also sampled from the OpenImage dataset and preprocessed using the same procedures as we employed for the training data. Since methods like PPT perform poorly with fine-grained masks, we dilate the mask with Open Computer Vision Library (OpenCV2) [27] with dilation kernel sizes as 50 and 100 for 512 and 1024 resolutions, respectively.

Model Training. We train RORem using the AdamW optimizer [34] with a learning rate of $5e-5$. In each round of training, we perform 50K optimization steps with a total training batch size of 192 across 16 NVIDIA A100 GPUs. The SDXL-inpainting model [42] is employed as the initial model for fine-tuning. During the training process, we set the text prompt to null, as it is unnecessary for our RORem.

Compared Methods. We compare RORem with state-of-the-art object removal methods, including Lama [54], SDXL-inpainting (SDXL-INP) [42], Inst-inpainting (INST)

[64], PowerPoint (PPT) [72], Instructpix2pix (IP2P) [4], CLIPAway [8], and DesignEdit [17]. Except for Lama, all the other methods leverage the pre-trained SD model. DesignEdit is a training-free method, built upon the noise inversion techniques and the inference framework of SD. For SDXL-inpainting, we employ LLava-1.6 [33] to generate captions for the background, and use them as text prompts for image completion. Note that we do not compare RORem with the ObjectDrop [59] and EmuEdit [51], as their source codes or models are not publicly available.

Evaluation Metrics. Following prior works [59, 64, 72], we employ the classical fidelity metric PSNR, alongside perceptual metrics DINO [40], CLIP [44], and LPIPS [69], to comprehensively assess the competing methods. Considering that these metrics may not be able to accurately reflect the practical object removal performance, we conduct a user study by inviting five volunteers. The volunteers are presented with the object removal outcomes generated by each method together with the original image and the mask. They are asked to determine whether the model output is a success or a failure, based on factors such as whether the object is completely removed and the quality of the object removed image. The success rate of each method is computed by averaging the results across all volunteers. The interface and more details of the user study can be found in the **Appendix A**. In addition, we also utilize our trained discriminator D_ϕ , which aims to approximate human judgment on the success or failure of object removal output, as another metric in the experiment.

4.2. Object Removal Results

As shown in Tab. 1, the size of our training dataset increases from the initial 60K pairs to the final 200K pairs. With more high quality training pairs, the removal success rate of our RORem model escalates from 7.6% to 76.2% on our test set. The visual examples of object removal results at each training round can be found in the **Appendix C**. One can see that with the expansion of training data, RORem gradually improves its object removal robustness and the removal quality. In the following, we compare our RORem model with its competitors quantitatively and qualitatively.

Quantitative Comparisons. The quantitative comparisons among the competing methods are presented in Tab. 2. We have the following observations. First, RORem demonstrates substantial improvements over previous methods in terms of success rate via user study. In particular, RORem's success rate is about 18% higher than the second best methods on both resolutions 512×512 and 1024×1024 . This validates the exceptional robustness of RORem. Lama works well when the image size is 512×512 , but its limited generative capacity makes it exhibit poor performance on higher resolution images. SDXL-based methods like SDXL-INP and DesignEdit perform better on 1024×1024

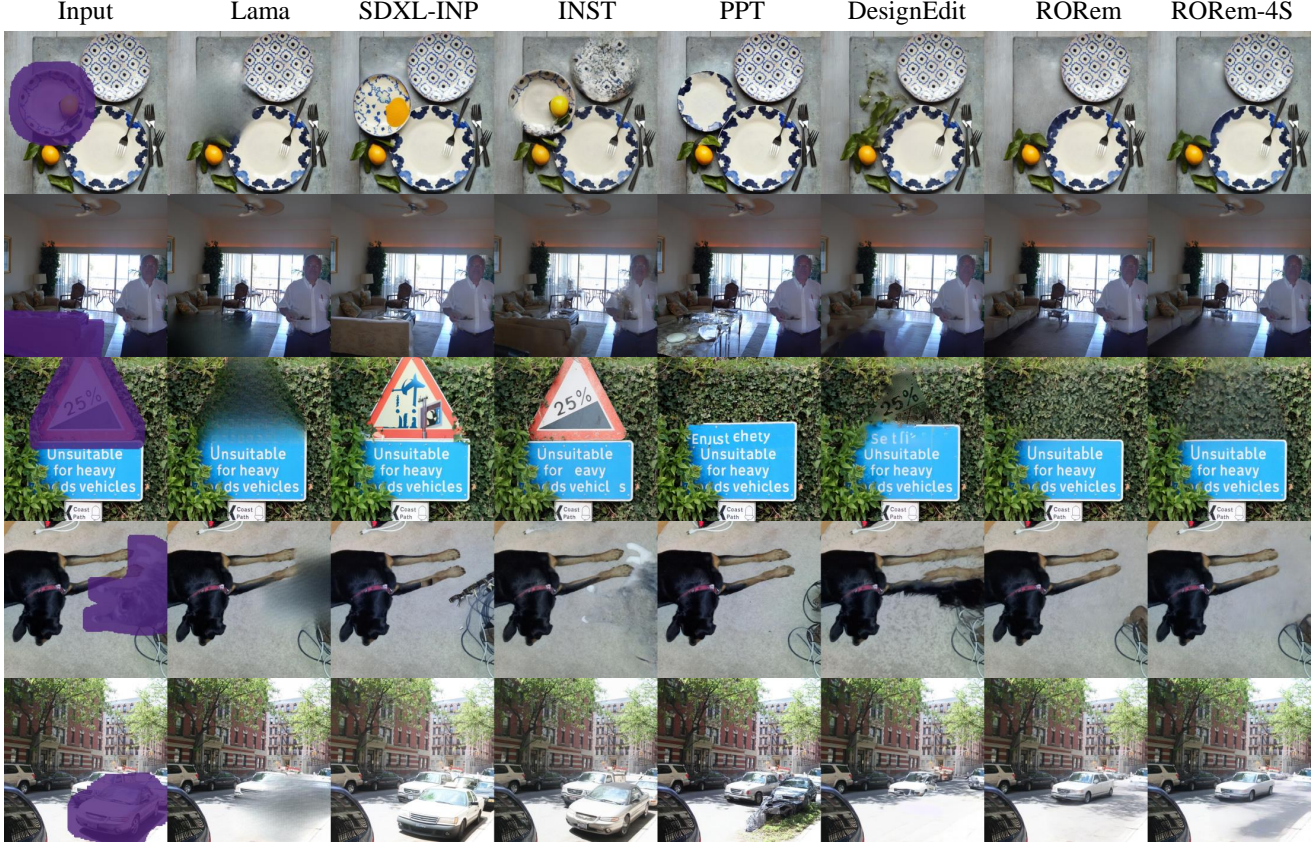


Figure 7. Visual comparison of the object removal results by RORem and other methods on 1024×1024 resolution images. One can see that there can be incomplete removal regions, blurry synthesis output, and incorrect synthesis contents in previous methods, while RORem demonstrates robust removal performance. Due to limited space, we put the visual results of IP2P, CLIPAway in the **Appendix D**.

resolution images but they lag much behind our RORem. Overall, the competing methods may achieve good results on some cases, but their robustness is rather limited. Similar trend can be observed when evaluating the success rates using our trained discriminator D_ϕ . Specifically, based on D_ϕ , RORem’s success rate is approximately 18% and 15% higher than the second-best methods at resolutions of 512×512 and 1024×1024 , respectively. Furthermore, we can see that the success rates estimated by D_ϕ closely align with human annotation in the test set (the deviation is less than 3% in most cases). This indicates that our trained D_ϕ effectively mirrors human preferences.

Second, RORem achieves the best PSNR metric among the diffusion-based methods, and it is only lower than Lama. This is because the diffusion-based methods utilize VAEs to compress images to the latent space, leading to some loss of details in the unmasked regions. Since Lama does not rely on diffusion models, it achieves high PSNR on unmasked regions. However, its inpainting quality on the masked region is not as good as RORem. Third, RORem achieves state-of-the-art performance in perceptual metrics, including LPIPS, DINO and CLIP score on both resolu-

tions, producing removal results that are more consistent with human perception. Finally, our distilled model with four diffusion steps, denoted by RORem-4S, achieves close performance to RORem but with a significant reduction in inference time from 4.03s and 4.44s to 0.50s and 0.83s per image (a reduction of 88% and 81%) on the two resolutions. Though there are some deterioration in PSNR and LPIPS, there is only a slight reduction in the success rate (1.4% and 2.8%). Overall, RORem-4S achieves the second best results in success rate, DINO, CLIP and inference time.

Qualitative Comparisons. The qualitative comparison on images of resolution 1024×1024 are illustrated in Fig. 7. We can see that Lama generates blurry synthesis output in most cases and exhibits poor generation quality. SDXL-INP and INST fail in most cases. The masked regions are partially removed (see images plate in row 1 and cat in row 4) or not removed (see images sign and car). PPT sometimes fills the masked regions with incorrect contents (see images sofa and car). Especially, the sign is inpainted with nonexistent words in row 3. While DesignEdit successfully removes the car in row 5, it suffers from visual artifacts in images sofa and sign. Meanwhile, the surrounding items

Image Size	Method	Success Rate (Human) \uparrow	Success Rate (D_ϕ) \uparrow	PSNR \uparrow	LPIPS \downarrow	DINO \uparrow	CLIP \uparrow	Time(s)
512 \times 512	Lama (WACV 2022 [54])	55.4	48.6	33.06	<u>2.99</u>	0.77	22.77	0.15
	SDXL-INO (ICLR 2024 [42])	15.8	16.0	26.03	4.72	<u>0.76</u>	22.23	4.52
	INST (ArXiv 2023 [64])	3.0	3.6	23.75	10.36	0.74	20.80	5.68
	PPT (ECCV 2024 [72])	55.8	56.8	28.41	6.06	0.75	22.36	1.98
	IP2P (CVPR 2023 [4])	10.0	7.2	19.81	19.95	0.72	13.82	3.62
	CLIPAway (NIPS 2024 [8])	32.4	35.4	28.69	3.55	22.91	0.75	4.95
	DesignEdit (ArXiv 2024 [17])	29.2	25.4	26.79	8.16	0.68	22.01	12.88
	RORRem	76.2	74.6	<u>31.10</u>	2.86	0.77	23.28	4.03
1024 \times 1024	RORRem-4S	<u>74.8</u>	<u>71.0</u>	30.08	3.47	0.77	<u>23.24</u>	<u>0.50</u>
	Lama (WACV 2022 [54])	18.2	13.8	36.36	2.68	0.75	22.24	0.21
	SDXL-INO (ICLR 2024 [42])	20.4	18.6	32.28	<u>1.59</u>	<u>0.77</u>	22.06	5.57
	INST (ArXiv 2023 [64])	3.2	3.6	24.83	9.42	<u>0.77</u>	20.65	6.75
	PPT (ECCV 2024 [72])	46.8	54.6	33.34	2.40	<u>0.77</u>	22.62	5.61
	IP2P (CVPR 2023 [4])	6.6	4.6	22.89	24.90	0.76	20.75	10.46
	CLIPAway (NIPS 2024 [8])	23.8	29.2	33.04	1.86	22.42	0.75	41.42
	DesignEdit (ArXiv 2024 [17])	52.4	56.8	32.98	2.73	<u>0.77</u>	22.97	23.11
	RORRem	70.2	71.6	<u>36.05</u>	1.44	0.78	23.14	4.44
	RORRem-4S	<u>67.4</u>	<u>68.2</u>	35.02	1.84	0.77	<u>23.03</u>	0.83

Table 2. The quantitative comparison of different object removal methods under two image resolutions. The best and second best results of each metric are highlighted in bold and underscore, respectively. RORRem-4S means our distilled RORRem model with 4 diffusion steps.

Method	Precision \uparrow	Recall \uparrow	F1 \uparrow	Acc. \uparrow
D_ϕ (Round 1)	0.833	0.528	0.646	0.685
D_ϕ (Round 2)	0.901	0.565	0.695	0.706
D_ϕ (Round 3)	0.987	0.466	0.633	0.680
D_ϕ (+Synthesized)	0.621	0.921	0.742	0.669
D_ϕ (+Annotated)	0.740	0.890	0.808	0.782
D_ϕ (+All)	0.821	0.840	0.830	0.823

Table 3. Performance of discriminator in different rounds. Acc. means Accuracy.

can impose negative impact on the synthesis output, leading to wrong filling contents in images plate and dog. In contrast, RORRem successfully removes the masked regions in all cases. Furthermore, our distilled RORRem-4S model also works well in just four diffusion steps. Due to limited space, we put the visual results on images of 512 \times 512 resolution in the Appendix E.

4.3. Training and Evaluation of Discriminator

In our dataset construction process, we train a discriminator D_ϕ to automate the training sample selection process. Therefore, it is necessary to evaluate whether the discrimination capability of D_ϕ is good enough to align with human preference. We use our human labeled test set to assess D_ϕ in this section, and the results are shown in Tab. 3. (For the definitions of precision, recall, F1 and accuracy, please refer to the Appendix B.)

Since high-quality removal samples are crucial for model

training, we choose the discriminator checkpoints with the highest precision and set a high threshold as 0.9. This can ensure that the selected removal pairs are of high-quality in each round of automation annotation. The performance of D_ϕ trained in the 3 rounds of automated annotation are presented in the top three rows of Tab. 3. In the initial stage, with a human feedback training dataset comprising 10K samples, the precision of D_ϕ is 0.833. As the training dataset expands, the discriminator's precision improves significantly, exceeding 0.98 in the last round. While the score on other metrics may not as good as the precision, this ensures that only the very high quality samples will be included in the training data expansion process.

After expanding the dataset, how to ensure the accuracy becomes crucial for reliable performance evaluation. We observe that while D_ϕ aligns well with human preferences when evaluating our RORRem, it exhibits bias in assessing other methods because D_ϕ is exposed only to the failure cases of RORRem during training. To make D_ϕ a good assessor for more competing methods, we expand the training data of it using several strategies, as detailed in Tab. 4. First, in addition to the human annotated 17,322 positive and 12,678 negative samples of RORRem, we sample 600 examples from our training dataset and edit them using the seven competing methods. The edited results are manually annotated, leading to 785 positive and 3,415 negative samples. Second, we apply various degradation (blur, noise, downsample and the mixture of them) and ‘no-change’ to the masked regions of RORRem editing outputs, generat-

	Annotated Data				Synthesized Data			
	RORem	Baselines	Blur	Noise	Downsample	Mixed	No-change	RORD
Positive	17,322	785	0	0	0	0	0	18,859
Negative	12,678	3,415	3,000	3,000	3,000	3,000	3,000	0
Total	30,000	4,200	3,000	3,000	3,000	3,000	3,000	18,859

Table 4. The details of our constructed dataset for training the final discriminator. ‘Baseline’ means the seven competing methods used in the experiments. ‘Mixed’ refers to the combination of Blur, Noise and Downsample degradations. ‘No-change’ indicates the use of the source image directly as the editing result.

ing 15,000 negative samples. Finally, we consider all the 18,859 pairs in the RORD dataset as positive samples.

With this enriched dataset, we fine-tune the discriminator D_ϕ for additional training rounds. We experiment with three settings: using synthesized data along with RORem annotated data, using baseline annotated data along with RORem annotated data, and using all the synthesized and annotated data as the training set. The performance of D_ϕ is presented in the three bottom rows of Tab. 3. Our results indicate that enriching the training data with synthesized samples improves recall, allowing D_ϕ to better recognize positive samples. By employing both synthesized and annotated data, we can further improve accuracy. Finally, by designating removal pairs with predicted scores lower than 0.35 as negative samples, the discriminator achieves an accuracy of 0.823. We then utilize this refined D_ϕ to evaluate the success rates of different methods, with results presented in Tab. 2. The results demonstrate that D_ϕ effectively aligns with human preferences.

5. Conclusion

We proposed RORem, a robust object removal model with human-in-the-loop during training. To assemble a large-scale, high-quality, and diverse removal dataset, we introduced a semi-supervised learning scheme that leverages both human and automatic annotations, ultimately building a dataset with 200K high-quality object removal pairs. Utilizing this dataset, we fine-tuned an SDXL-based inpainting model into a reliable removal model, which was further distilled into four diffusion steps to facilitate inference speed. Experimental results demonstrated the outstanding object removal performance of RORem. In specific, it achieved about 18% higher success rate than previous methods on two different resolutions.

Despite its clear advantages, RORem has certain limitations. First, due to the inherent problems of VAEs in image detail compression, the image quality of unmasked regions may suffer some degradation. Second, RORem encounters challenges in achieving satisfactory results when the background contains human fingers and small faces (see the **Appendix F** for visual examples), which is also a known problem for many generative diffusion models.

References

- [1] Abubakar Abid, Ali Abdalla, Ali Abid, Dawood Khan, Abdurrahman Alfozan, and James Zou. Gradio: Hassle-free sharing and testing of ml models in the wild. *arXiv preprint arXiv:1906.02569*, 2019. 1
- [2] Eirikur Agustsson and Radu Timofte. Ntire 2017 challenge on single image super-resolution: Dataset and study. In *The IEEE Conference on Computer Vision and Pattern Recognition (CVPR) Workshops*, 2017. 5, 3
- [3] Andreas Blattmann, Tim Dockhorn, Sumith Kulal, Daniel Mendelevitch, Maciej Kilian, Dominik Lorenz, Yam Levi, Zion English, Vikram Voleti, Adam Letts, et al. Stable video diffusion: Scaling latent video diffusion models to large datasets. *arXiv preprint arXiv:2311.15127*, 2023. 3
- [4] Tim Brooks, Aleksander Holynski, and Alexei A Efros. Instructpix2pix: Learning to follow image editing instructions. In *Proceedings of the IEEE/CVF Conference on Computer Vision and Pattern Recognition*, pages 18392–18402, 2023. 3, 6, 8
- [5] Chenjie Cao, Qiaole Dong, and Yanwei Fu. Zits++: Image inpainting by improving the incremental transformer on structural priors. *IEEE Transactions on Pattern Analysis and Machine Intelligence*, 45(10):12667–12684, 2023. 3
- [6] Antonio Criminisi, Patrick Pérez, and Kentaro Toyama. Region filling and object removal by exemplar-based image inpainting. *IEEE Transactions on image processing*, 13(9):1200–1212, 2004. 1
- [7] Qiaole Dong, Chenjie Cao, and Yanwei Fu. Incremental transformer structure enhanced image inpainting with masking positional encoding. In *Proceedings of the IEEE/CVF Conference on Computer Vision and Pattern Recognition*, pages 11358–11368, 2022. 1, 3
- [8] Yigit Ekin, Ahmet Burak Yildirim, Erdem Eren Caglar, Aykut Erdem, Erkut Erdem, and Aysegul Dundar. Clipaway: Harmonizing focused embeddings for removing objects via diffusion models. *arXiv preprint arXiv:2406.09368*, 2024. 6, 8
- [9] Patrick Esser, Sumith Kulal, Andreas Blattmann, Rahim Entezari, Jonas Müller, Harry Saini, Yam Levi, Dominik Lorenz, Axel Sauer, Frederic Boesel, et al. Scaling rectified flow transformers for high-resolution image synthesis. In *Forty-first International Conference on Machine Learning*, 2024. 3
- [10] Zigang Geng, Binxin Yang, Tiansai Hang, Chen Li, Shuyang Gu, Ting Zhang, Jianmin Bao, Zheng Zhang, Houqiang Li, 9

Han Hu, et al. Instructdiffusion: A generalist modeling interface for vision tasks. In *Proceedings of the IEEE/CVF Conference on Computer Vision and Pattern Recognition*, pages 12709–12720, 2024. 3

[11] Ian Goodfellow, Jean Pouget-Abadie, Mehdi Mirza, Bing Xu, David Warde-Farley, Sherjil Ozair, Aaron Courville, and Yoshua Bengio. Generative adversarial networks. *Communications of the ACM*, 63(11):139–144, 2020. 3

[12] Lanqing Guo, Chong Wang, Wenhan Yang, Siyu Huang, Yufei Wang, Hanspeter Pfister, and Bihan Wen. Shadowdiffusion: When degradation prior meets diffusion model for shadow removal. In *Proceedings of the IEEE/CVF Conference on Computer Vision and Pattern Recognition*, pages 14049–14058, 2023. 1

[13] Ligong Han, Song Wen, Qi Chen, Zhixing Zhang, Kunpeng Song, Mengwei Ren, Ruijiang Gao, Anastasis Stathopoulos, Xiaoxiao He, Yuxiao Chen, et al. Proxedit: Improving tuning-free real image editing with proximal guidance. In *Proceedings of the IEEE/CVF Winter Conference on Applications of Computer Vision*, pages 4291–4301, 2024. 3

[14] Amir Hertz, Ron Mokady, Jay Tenenbaum, Kfir Aberman, Yael Pritch, and Daniel Cohen-Or. Prompt-to-prompt image editing with cross attention control. *arXiv preprint arXiv:2208.01626*, 2022. 3

[15] Jonathan Ho, Ajay Jain, and Pieter Abbeel. Denoising diffusion probabilistic models. *Advances in neural information processing systems*, 33:6840–6851, 2020. 3, 5

[16] Edward J Hu, Yelong Shen, Phillip Wallis, Zeyuan Allen-Zhu, Yuanzhi Li, Shean Wang, Lu Wang, and Weizhu Chen. Lora: Low-rank adaptation of large language models. *arXiv preprint arXiv:2106.09685*, 2021. 4

[17] Yueru Jia, Yuhui Yuan, Aosong Cheng, Chuke Wang, Ji Li, Huizhu Jia, and Shanghang Zhang. Designedit: Multi-layered latent decomposition and fusion for unified & accurate image editing. *arXiv preprint arXiv:2403.14487*, 2024. 3, 6, 8

[18] Alexander Kirillov, Eric Mintun, Nikhila Ravi, Hanzi Mao, Chloe Rolland, Laura Gustafson, Tete Xiao, Spencer Whitehead, Alexander C Berg, Wan-Yen Lo, et al. Segment anything. In *Proceedings of the IEEE/CVF International Conference on Computer Vision*, pages 4015–4026, 2023. 5

[19] Keunsoo Ko and Chang-Su Kim. Continuously masked transformer for image inpainting. In *Proceedings of the IEEE/CVF International Conference on Computer Vision*, pages 13169–13178, 2023. 1, 3

[20] Alina Kuznetsova, Hassan Rom, Neil Alldrin, Jasper Uijlings, Ivan Krasin, Jordi Pont-Tuset, Shahab Kamali, Stefan Popov, Matteo Malloci, Alexander Kolesnikov, et al. The open images dataset v4: Unified image classification, object detection, and visual relationship detection at scale. *International journal of computer vision*, 128(7):1956–1981, 2020. 2, 4, 6

[21] Avisek Lahiri, Arnav Kumar Jain, Sanskar Agrawal, Pabitra Mitra, and Prabir Kumar Biswas. Prior guided gan based semantic inpainting. In *Proceedings of the IEEE/CVF conference on computer vision and pattern recognition*, pages 13696–13705, 2020. 1

[22] Jiabao Lei, Jiapeng Tang, and Kui Jia. Rgbd2: Generative scene synthesis via incremental view inpainting using rgbd diffusion models. In *Proceedings of the IEEE/CVF Conference on Computer Vision and Pattern Recognition*, pages 8422–8434, 2023. 1

[23] Jingyuan Li, Ning Wang, Lefei Zhang, Bo Du, and Dacheng Tao. Recurrent feature reasoning for image inpainting. In *Proceedings of the IEEE/CVF conference on computer vision and pattern recognition*, pages 7760–7768, 2020. 3

[24] Ruibin Li, Jingcai Guo, Song Guo, Qihua Zhou, and Jie Zhang. Freepih: Training-free painterly image harmonization with diffusion model. *CoRR*, abs/2311.14926, 2023. 1

[25] Ruibin Li, Ruihuang Li, Song Guo, and Lei Zhang. Source prompt disentangled inversion for boosting image editability with diffusion models. In *European Conference on Computer Vision*, 2024. 3

[26] Wenbo Li, Zhe Lin, Kun Zhou, Lu Qi, Yi Wang, and Jiaya Jia. Mat: Mask-aware transformer for large hole image inpainting. In *Proceedings of the IEEE/CVF conference on computer vision and pattern recognition*, pages 10758–10768, 2022. 1, 3

[27] Open Computer Vision Library. Cv2 dilate function, 2024. 6

[28] Tsung-Yi Lin, Michael Maire, Serge Belongie, James Hays, Pietro Perona, Deva Ramanan, Piotr Dollár, and C Lawrence Zitnick. Microsoft coco: Common objects in context. In *Computer Vision–ECCV 2014: 13th European Conference, Zurich, Switzerland, September 6–12, 2014, Proceedings, Part V 13*, pages 740–755. Springer, 2014. 2, 3

[29] Guilin Liu, Fitzsum A Reda, Kevin J Shih, Ting-Chun Wang, Andrew Tao, and Bryan Catanzaro. Image inpainting for irregular holes using partial convolutions. In *Proceedings of the European conference on computer vision (ECCV)*, pages 85–100, 2018. 3

[30] Hongyu Liu, Bin Jiang, Yi Xiao, and Chao Yang. Coherent semantic attention for image inpainting. In *Proceedings of the IEEE/CVF international conference on computer vision*, pages 4170–4179, 2019. 3

[31] Hongyu Liu, Bin Jiang, Yibing Song, Wei Huang, and Chao Yang. Rethinking image inpainting via a mutual encoder-decoder with feature equalizations. In *Computer Vision–ECCV 2020: 16th European Conference, Glasgow, UK, August 23–28, 2020, Proceedings, Part II 16*, pages 725–741. Springer, 2020. 1, 3

[32] Hongyu Liu, Ziyu Wan, Wei Huang, Yibing Song, Xintong Han, and Jing Liao. Pd-gan: Probabilistic diverse gan for image inpainting. In *Proceedings of the IEEE/CVF conference on computer vision and pattern recognition*, pages 9371–9381, 2021. 1

[33] Haotian Liu, Chunyuan Li, Qingyang Wu, and Yong Jae Lee. Visual instruction tuning. *Advances in neural information processing systems*, 36, 2024. 6

[34] I Loshchilov. Decoupled weight decay regularization. *arXiv preprint arXiv:1711.05101*, 2017. 6

[35] Andreas Lugmayr, Martin Danelljan, Andres Romero, Fisher Yu, Radu Timofte, and Luc Van Gool. Repaint: Inpainting using denoising diffusion probabilistic models. In *Proceedings of the IEEE/CVF conference on computer vision and pattern recognition*, pages 11461–11471, 2022. 1, 3

[36] Simian Luo, Yiqin Tan, Longbo Huang, Jian Li, and Hang Zhao. Latent consistency models: Synthesizing high-resolution images with few-step inference. *arXiv preprint arXiv:2310.04378*, 2023. [2](#), [5](#)

[37] Yuqing Ma, Xianglong Liu, Shihao Bai, Lei Wang, Aishan Liu, Dacheng Tao, and Edwin R Hancock. Regionwise generative adversarial image inpainting for large missing areas. *IEEE transactions on cybernetics*, 53(8):5226–5239, 2022. [1](#), [3](#)

[38] Gaël Mahfoudi, Badr Tajini, Florent Retraint, Frederic Morain-Nicolier, Jean Luc Dugelay, and PIC Marc. Defacto: Image and face manipulation dataset. In *2019 27Th european signal processing conference (EUSIPCO)*, pages 1–5. IEEE, 2019. [3](#)

[39] Ron Mokady, Amir Hertz, Kfir Aberman, Yael Pritch, and Daniel Cohen-Or. Null-text inversion for editing real images using guided diffusion models. *arXiv preprint arXiv:2211.09794*, 2022. [3](#)

[40] Maxime Oquab, Timothée Darcet, Théo Moutakanni, Huy Vo, Marc Szafraniec, Vasil Khalidov, Pierre Fernandez, Daniel Haziza, Francisco Massa, Alaaeldin El-Nouby, et al. Dinov2: Learning robust visual features without supervision. *arXiv preprint arXiv:2304.07193*, 2023. [6](#)

[41] Deepak Pathak, Philipp Krahenbuhl, Jeff Donahue, Trevor Darrell, and Alexei A Efros. Context encoders: Feature learning by inpainting. In *Proceedings of the IEEE conference on computer vision and pattern recognition*, pages 2536–2544, 2016. [1](#), [3](#)

[42] Dustin Podell, Zion English, Kyle Lacey, Andreas Blattmann, Tim Dockhorn, Jonas Müller, Joe Penna, and Robin Rombach. Sdxl: Improving latent diffusion models for high-resolution image synthesis. *arXiv preprint arXiv:2307.01952*, 2023. [1](#), [2](#), [3](#), [4](#), [6](#), [8](#)

[43] Weize Quan, Jiaxi Chen, Yanli Liu, Dong-Ming Yan, and Peter Wonka. Deep learning-based image and video inpainting: A survey. *International Journal of Computer Vision*, 132(7): 2367–2400, 2024. [1](#)

[44] Alec Radford, Jong Wook Kim, Chris Hallacy, Aditya Ramesh, Gabriel Goh, Sandhini Agarwal, Girish Sastry, Amanda Askell, Pamela Mishkin, Jack Clark, et al. Learning transferable visual models from natural language supervision. In *International conference on machine learning*, pages 8748–8763. PMLR, 2021. [6](#)

[45] Robin Rombach, Andreas Blattmann, Dominik Lorenz, Patrick Esser, and Björn Ommer. High-resolution image synthesis with latent diffusion models. In *Proceedings of the IEEE/CVF conference on computer vision and pattern recognition*, pages 10684–10695, 2022. [3](#)

[46] Olaf Ronneberger, Philipp Fischer, and Thomas Brox. U-net: Convolutional networks for biomedical image segmentation. In *Medical image computing and computer-assisted intervention–MICCAI 2015: 18th international conference, Munich, Germany, October 5-9, 2015, proceedings, part III 18*, pages 234–241. Springer, 2015. [3](#)

[47] Min-Cheol Sagong, Yoon-Jae Yeo, Seung-Won Jung, and Sung-Jea Ko. Rord: A real-world object removal dataset. In *BMVC*, page 542, 2022. [1](#), [2](#), [3](#), [6](#)

[48] Chitwan Saharia, William Chan, Huiwen Chang, Chris Lee, Jonathan Ho, Tim Salimans, David Fleet, and Mohammad Norouzi. Palette: Image-to-image diffusion models. In *ACM SIGGRAPH 2022 conference proceedings*, pages 1–10, 2022. [1](#), [3](#)

[49] Christoph Schuhmann, Romain Beaumont, Richard Vencu, Cade Gordon, Ross Wightman, Mehdi Cherti, Theo Coombes, Aarush Katta, Clayton Mullis, Mitchell Wortsman, et al. Laion-5b: An open large-scale dataset for training next generation image-text models. *Advances in Neural Information Processing Systems*, 35:25278–25294, 2022. [2](#), [4](#)

[50] Pourya Shamsolmoali, Masoumeh Zareapoor, and Eric Granger. Transinpaint: Transformer-based image inpainting with context adaptation. In *Proceedings of the IEEE/CVF International Conference on Computer Vision*, pages 849–858, 2023. [1](#), [3](#)

[51] Shelly Sheynin, Adam Polyak, Uriel Singer, Yuval Kirstain, Amit Zohar, Oron Ashual, Devi Parikh, and Yaniv Taigman. Emu edit: Precise image editing via recognition and generation tasks. In *Proceedings of the IEEE/CVF Conference on Computer Vision and Pattern Recognition*, pages 8871–8879, 2024. [3](#), [6](#)

[52] Jiaming Song, Chenlin Meng, and Stefano Ermon. Denoising diffusion implicit models. *arXiv preprint arXiv:2010.02502*, 2020. [3](#), [5](#)

[53] Yuhang Song, Chao Yang, Zhe Lin, Xiaofeng Liu, Qin Huang, Hao Li, and C-C Jay Kuo. Contextual-based image inpainting: Infer, match, and translate. In *Proceedings of the European conference on computer vision (ECCV)*, pages 3–19, 2018. [3](#)

[54] Roman Suvorov, Elizaveta Logacheva, Anton Mashikhin, Anastasia Remizova, Arsenii Ashukha, Aleksei Silvestrov, Naejin Kong, Harshith Goka, Kiwoong Park, and Victor Lempitsky. Resolution-robust large mask inpainting with fourier convolutions. In *Proceedings of the IEEE/CVF winter conference on applications of computer vision*, pages 2149–2159, 2022. [1](#), [3](#), [6](#), [8](#)

[55] Radu Timofte, Eirikur Agustsson, Luc Van Gool, Ming-Hsuan Yang, and Lei Zhang. Ntire 2017 challenge on single image super-resolution: Methods and results. In *Proceedings of the IEEE conference on computer vision and pattern recognition workshops*, pages 114–125, 2017. [5](#), [3](#)

[56] Petru-Daniel Tudosiu, Yongxin Yang, Shifeng Zhang, Fei Chen, Steven McDonagh, Gerasimos Lampouras, Ignacio Iacobacci, and Sarah Parisot. Mulan: A multi layer annotated dataset for controllable text-to-image generation. In *Proceedings of the IEEE/CVF Conference on Computer Vision and Pattern Recognition*, pages 22413–22422, 2024. [1](#), [2](#), [3](#), [6](#)

[57] Chaoyue Wang, Chang Xu, Chaohui Wang, and Dacheng Tao. Perceptual adversarial networks for image-to-image transformation. *IEEE Transactions on Image Processing*, 27(8):4066–4079, 2018. [1](#)

[58] Su Wang, Chitwan Saharia, Ceslee Montgomery, Jordi Pont-Tuset, Shai Noy, Stefano Pellegrini, Yasumasa Onoe, Sarah Laszlo, David J Fleet, Radu Soricu, et al. Imagen editor

and editbench: Advancing and evaluating text-guided image inpainting. In *Proceedings of the IEEE/CVF conference on computer vision and pattern recognition*, pages 18359–18369, 2023. 3

[59] Daniel Winter, Matan Cohen, Shlomi Fruchter, Yael Pritch, Alex Rav-Acha, and Yedid Hoshen. Objectdrop: Bootstrapping counterfactuals for photorealistic object removal and insertion. *arXiv preprint arXiv:2403.18818*, 2024. 1, 3, 4, 6

[60] Shaoan Xie, Zhifei Zhang, Zhe Lin, Tobias Hinz, and Kun Zhang. Smartbrush: Text and shape guided object inpainting with diffusion model. In *Proceedings of the IEEE/CVF Conference on Computer Vision and Pattern Recognition*, pages 22428–22437, 2023. 1

[61] Zhaoyi Yan, Xiaoming Li, Mu Li, Wangmeng Zuo, and Shiguang Shan. Shift-net: Image inpainting via deep feature rearrangement. In *Proceedings of the European conference on computer vision (ECCV)*, pages 1–17, 2018. 3

[62] Chao Yang, Xin Lu, Zhe Lin, Eli Shechtman, Oliver Wang, and Hao Li. High-resolution image inpainting using multi-scale neural patch synthesis. In *Proceedings of the IEEE conference on computer vision and pattern recognition*, pages 6721–6729, 2017. 3

[63] Raymond A Yeh, Chen Chen, Teck Yian Lim, Alexander G Schwing, Mark Hasegawa-Johnson, and Minh N Do. Semantic image inpainting with deep generative models. In *Proceedings of the IEEE conference on computer vision and pattern recognition*, pages 5485–5493, 2017. 3

[64] Ahmet Burak Yildirim, Vedat Baday, Erkut Erdem, Aykut Erdem, and Aysegul Dundar. Inst-inpaint: Instructing to remove objects with diffusion models. *arXiv preprint arXiv:2304.03246*, 2023. 1, 3, 6, 8

[65] Jiahui Yu, Zhe Lin, Jimei Yang, Xiaohui Shen, Xin Lu, and Thomas S Huang. Generative image inpainting with contextual attention. In *Proceedings of the IEEE conference on computer vision and pattern recognition*, pages 5505–5514, 2018. 3

[66] Yingchen Yu, Fangneng Zhan, Rongliang Wu, Jianxiong Pan, Kaiwen Cui, Shijian Lu, Feiying Ma, Xuansong Xie, and Chunyan Miao. Diverse image inpainting with bidirectional and autoregressive transformers. In *Proceedings of the 29th ACM International Conference on Multimedia*, pages 69–78, 2021. 3

[67] Yanhong Zeng, Jianlong Fu, Hongyang Chao, and Baining Guo. Learning pyramid-context encoder network for high-quality image inpainting. In *Proceedings of the IEEE/CVF conference on computer vision and pattern recognition*, pages 1486–1494, 2019. 3

[68] Yanhong Zeng, Jianlong Fu, and Hongyang Chao. Learning joint spatial-temporal transformations for video inpainting. In *Computer Vision–ECCV 2020: 16th European Conference, Glasgow, UK, August 23–28, 2020, Proceedings, Part XVI 16*, pages 528–543. Springer, 2020. 1

[69] Richard Zhang, Phillip Isola, Alexei A Efros, Eli Shechtman, and Oliver Wang. The unreasonable effectiveness of deep features as a perceptual metric. In *Proceedings of the IEEE conference on computer vision and pattern recognition*, pages 586–595, 2018. 6

[70] Shu Zhang, Xinyi Yang, Yihao Feng, Can Qin, Chia-Chih Chen, Ning Yu, Zeyuan Chen, Huan Wang, Silvio Savarese, Stefano Ermon, et al. Hive: Harnessing human feedback for instructional visual editing. In *Proceedings of the IEEE/CVF Conference on Computer Vision and Pattern Recognition*, pages 9026–9036, 2024. 3

[71] Shangchen Zhou, Chongyi Li, Kelvin CK Chan, and Chen Change Loy. Propainter: Improving propagation and transformer for video inpainting. In *Proceedings of the IEEE/CVF International Conference on Computer Vision*, pages 10477–10486, 2023. 3

[72] Junhao Zhuang, Yanhong Zeng, Wenran Liu, Chun Yuan, and Kai Chen. A task is worth one word: Learning with task prompts for high-quality versatile image inpainting. *arXiv preprint arXiv:2312.03594*, 2023. 1, 3, 6, 8

RORem: Training a Robust Object Remover with Human-in-the-Loop

Supplementary Material

In this supplementary file, we provide the following materials:

- The interface and more details of the user study (referring to Sec. 4.1 in the main paper);
- Details of the evaluation metrics for the discriminator (referring to Sec. 4.1 and Sec. 4.3 in the main paper);
- Visual examples of object removal results at each training round (referring to Sec 4.2 in the main paper);
- Visual results of IP2P and CLIPAway (referring to Sec 4.2 and Fig. 7 in the main paper);
- Visual results on images of 512×512 resolution (referring to Sec 4.2 in the main paper);
- Failure cases (referring to Sec. 5 in the main paper).

A. Annotation page and user study page

We design a webpage based on the open-source library Gradio [1] to conduct the human annotation (referring to Sec. 3.2 in the main paper) and the final human evaluation (referring to Sec. 4.1 in the main paper). Annotators are provided with the original images, the mask images and the object removal results, as illustrated in Fig. 8. They are asked to provide feedback by clicking the **Yes** or **No** button at the bottom right corner.

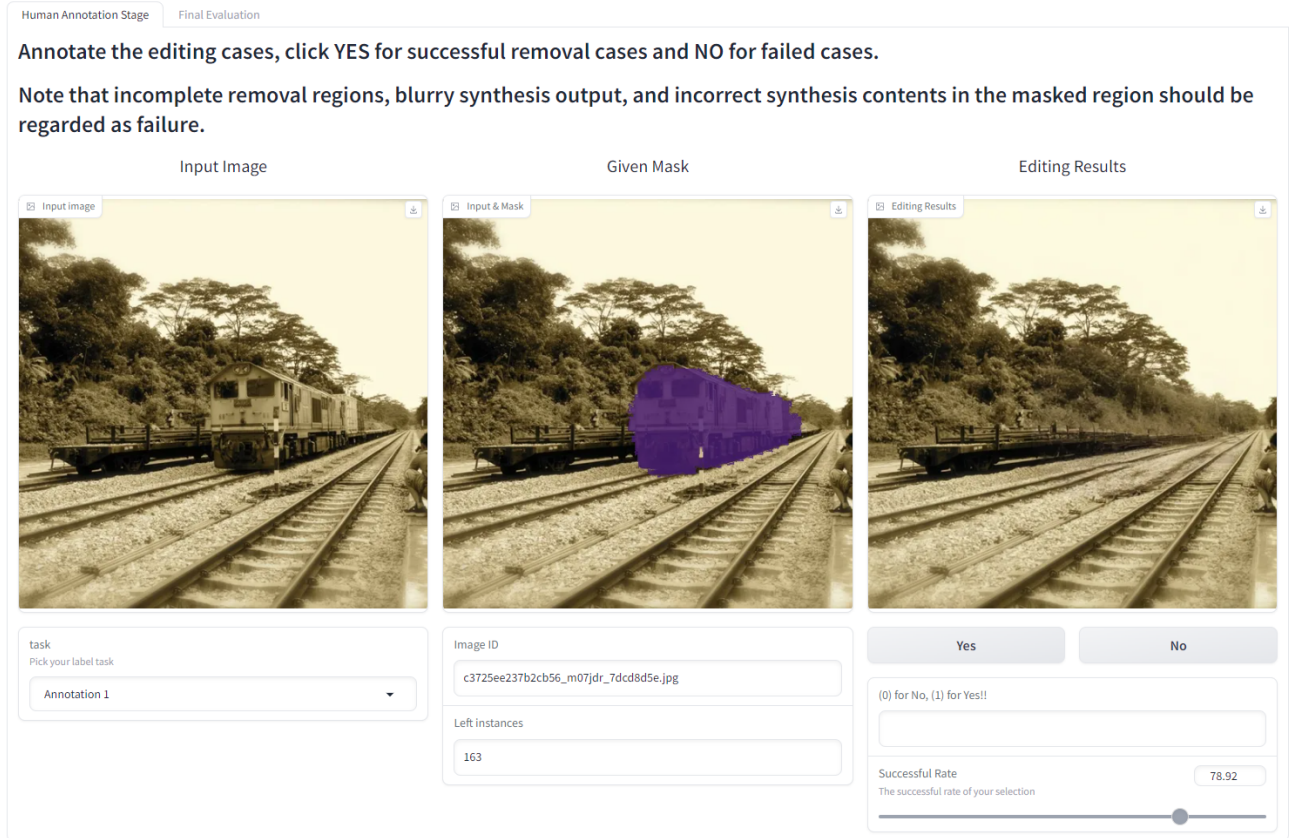


Figure 8. The interface for human annotation. The annotators are asked to give feedback by clicking "Yes" or "No" button.

The interface for final human evaluation is shown in Fig. 9. The input images and the masked images are displayed in the left column. The editing results of different methods as displayed in the right columns. Annotators are asked to click the multiple-choice check-boxes to select the successful removal results among different methods and submit the results.

We randomly shuffle the display order in each evaluation. Five volunteers participated in the final evaluation, and each volunteer annotated 1,000 samples, including 500 pairs of object removal cases under 512×512 resolution and 500 pairs under 1024×1024 resolution. We calculate the average success rate for different methods based on these human evaluations.

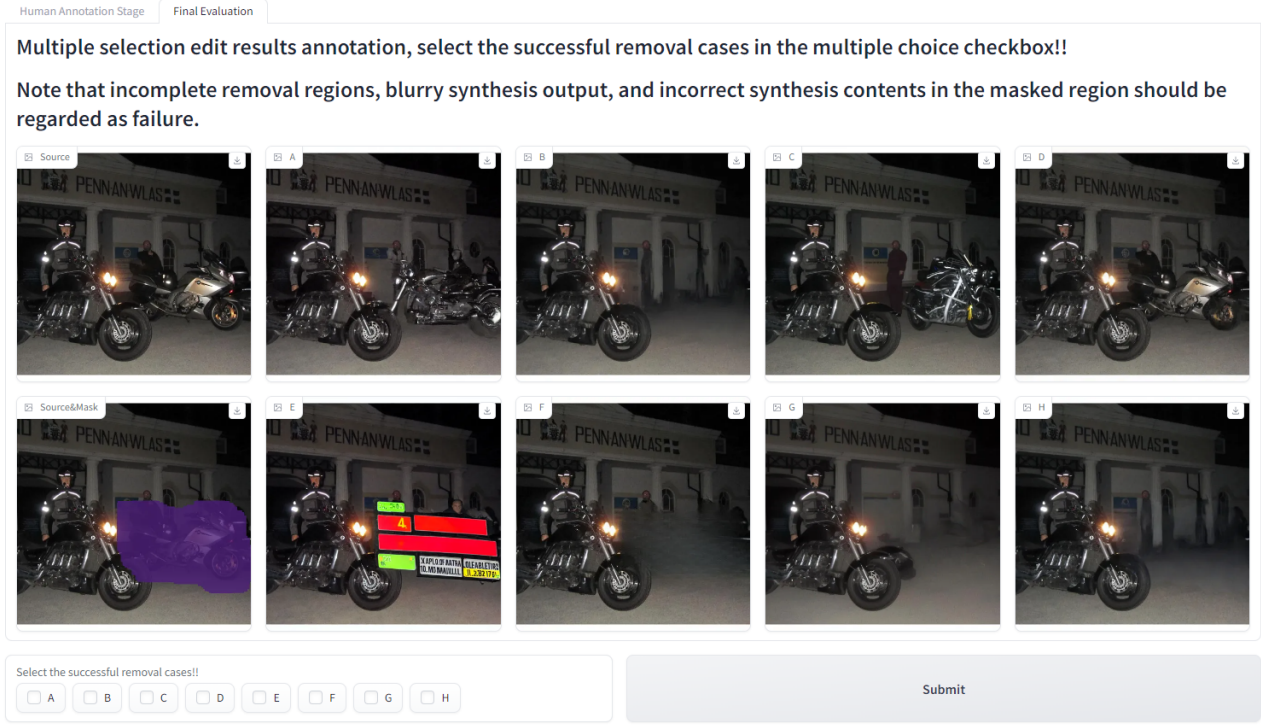


Figure 9. The interface for human evaluation. The volunteers make selections by checking the multiple-choice check-boxes at the bottom left corner.

B. The evaluation metrics for the discriminator

		Human Annotation Label		Precision = $\frac{TP}{TP+FP}$	Recall = $\frac{TP}{TP+FN}$	F1 = $\frac{2 \cdot Precision \cdot Recall}{Precision + Recall}$
		P	N			
Discriminator Predict Label	Y	True Positives	False Positives			
	N	False Negatives	True Negatives			

Figure 10. Confusion matrix and the definition of metrics for evaluating our discriminator.

We use the 500 pairs in the test set with 512×512 resolution to test the discriminator. The edited results are generated by our RORem. The definitions of precision, recall, F1 and accuracy are illustrated in Fig. 10. Among these metrics, precision represents the percentage of the true positive samples to the total positive samples predicted by our discriminator. High precision ensures that the selected removal pairs are all of high-quality. By setting the threshold as 0.9, our final discriminator can reach a precision of 0.983, which allows us to obtain a large amount of high-quality data pairs.

C. Visual examples of object removal results at each training round

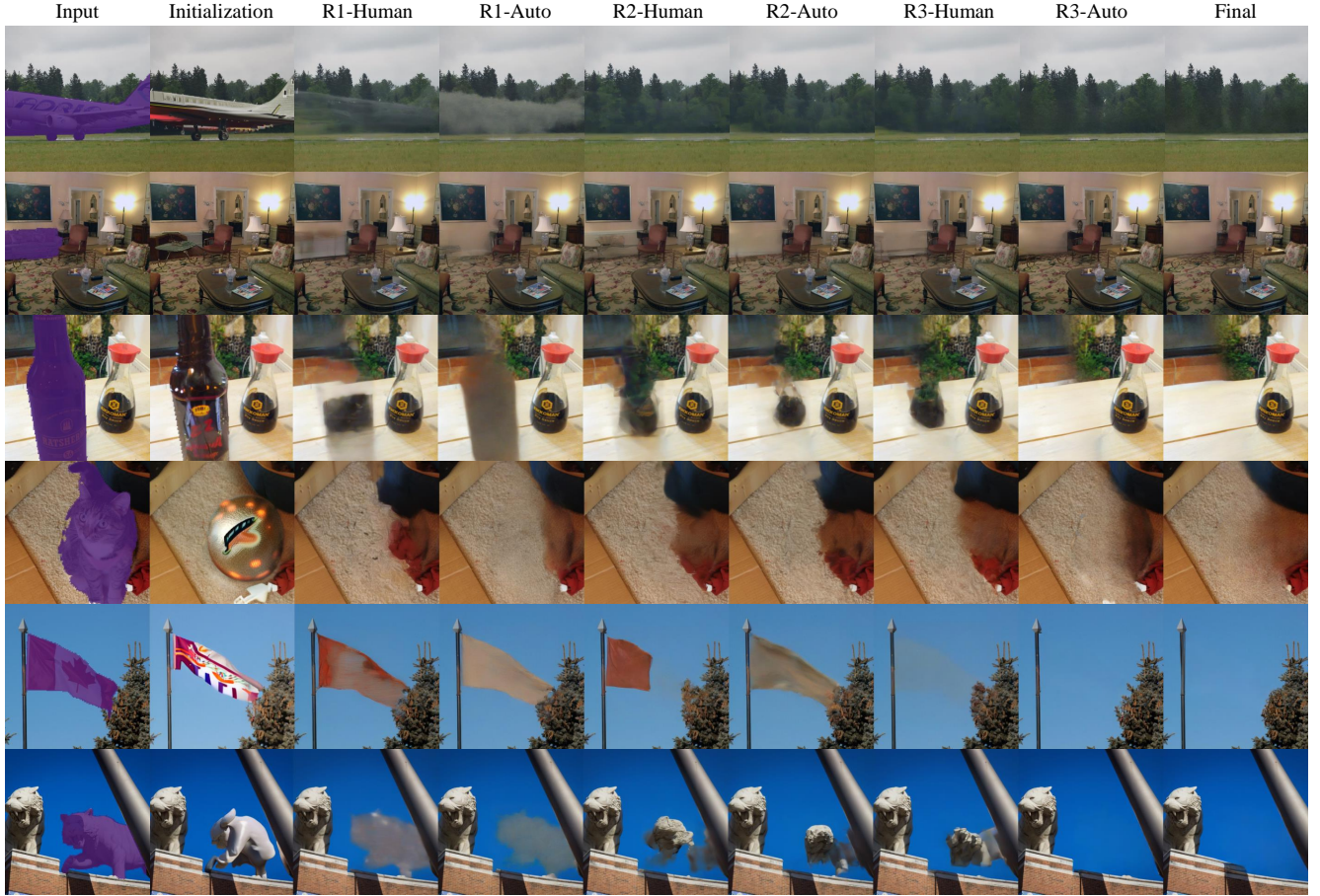


Figure 11. Visual results of RORem at each training round, one can see that the removal capacity of RORem improves with the increase of the dataset.

The visual examples of object removal results at each training round are provided in Fig. 11. We can see that the initial model SDXL-inpainting [42] always fills the masked regions with semantically similar contents instead of removing it (column Initialization). After the first round of finetuning, RORem can successfully remove the selected sofa (row 2) and cat (row 4); however, its removal capacity is not good enough, leading to failures in other cases (see partial removal cases bottle, statue and blurry synthesis case airplane). After we extend the training dataset and conduct more finetuning rounds (see column R1-Human to column R3-Auto), RORem can successfully remove the masked regions in most cases. Finally, we collect images with 2K resolution from DIV2K [2] and Flickr2K [55] to conduct the final stage finetuning, where the removal capacity of RORem can be well preserved (see column Final) and the image quality can be improved (see Tab. 1 in the main paper).

D. Visual results of IP2P and CLIPAway

The visual editing results of IP2P and CLIPAway on images of resolution of 1024×1024 are illustrated in Fig. 12. We can see that IP2P fails in all cases and even changes the overall style of the given images (see images plate in column 1 and car in column 5). CLIPAway exhibits the same problem as PPT, which often fills the masked regions with incorrect contents (see images sofa, dog and car).



Figure 12. Visual results of IP2P and CLIPAway on 1024×1024 resolution images.

E. Visual results on images of 512×512 resolution

The qualitative comparisons on images of 512×512 resolution are illustrated in Fig. 13. We can see that Lama can generate blurry synthesis outputs in some cases (see images koala in column 4 and plate in column 6). SDXL-INP, IP2P and INST fail in most cases. Moreover, as INST and IP2P are text-driven removal methods, the ambiguity of text instructions can lead to removal failures of selected objects (see images hot air balloon in column 3 and cup cake in column 6). IP2P not only fails to remove the select objects but also changes the overall style and details of the original images (see images hot air balloon, koala, and cup cake). PPT and CLIPAway can fill the masked regions with nonexistent contents in images bird (column 1), koala (column 4) and statue (column 5). DesignEdit succeeds in the first two removal cases, however it suffers from visual artifacts (see images koala, plate). In contrast, RORem successfully removes the selected objects in most cases. Meanwhile, our distilled RORem-4S model also works well in these cases with less time overhead.

F. Failure Cases

As we stated in the conclusion section of the main paper, although RORem achieves great improvement on the overall removal performance, it may fail in cases when the background contains human fingers and faces. Some failure cases are depicted in Fig. 14. Future work will be conducted for further improving the performance of RORem on these editing scenarios.

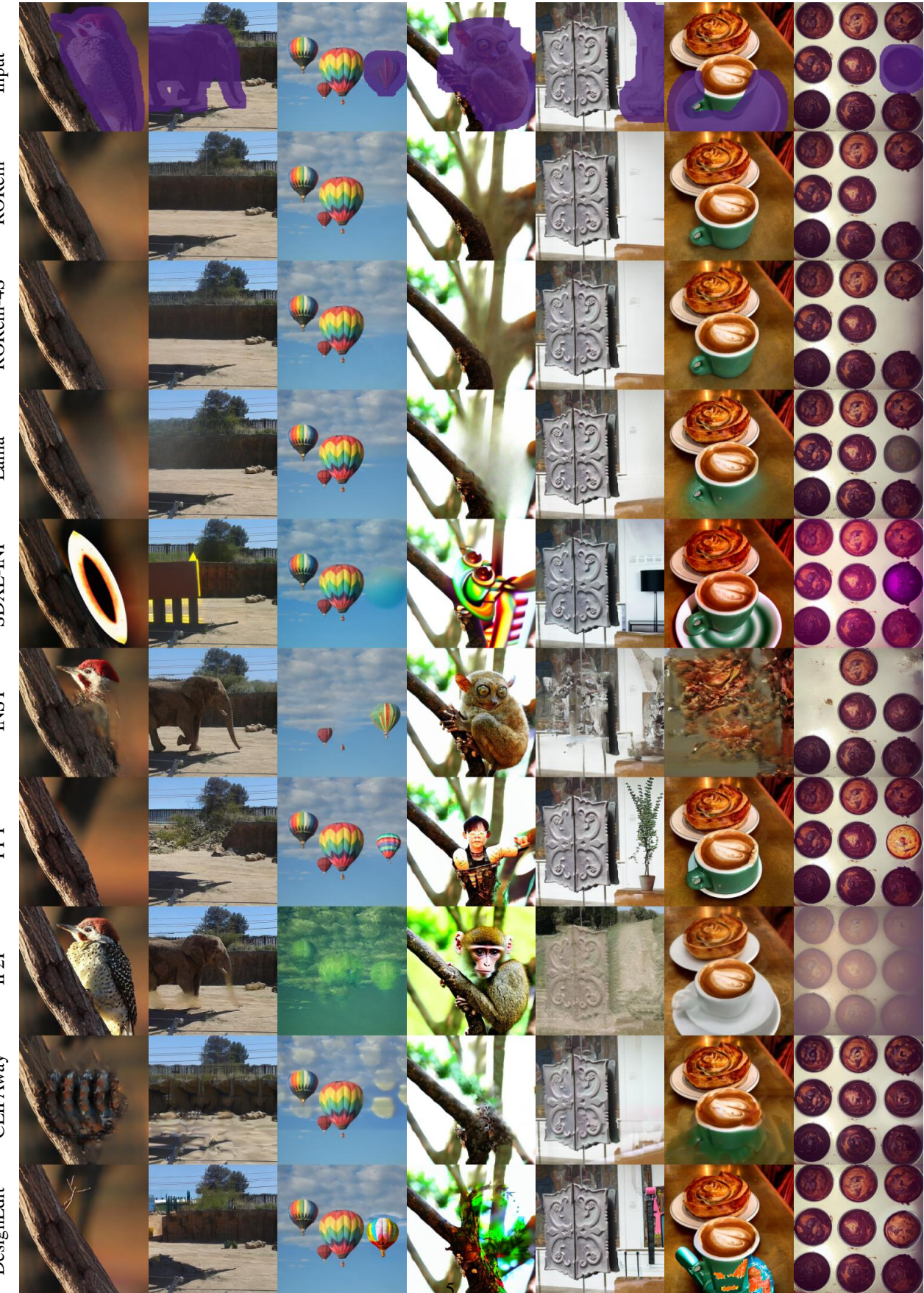


Figure 13. Visual comparison of the object removal results by RORem and other methods on 512×512 resolution images. One can see there can be incomplete removal regions, blurry synthesis output, wrong removal target, and incorrect synthesize contents in previous methods, while RORem demonstrate robust removal performance.



Figure 14. Failure cases of RORem.